Improved thermoelectric performance of (Zr0.3Hf0.7)NiSn half-Heusler compounds by Ta substitution

Krzysztof Gałązka, Sascha Populoh, Wenjie Xie, Songhak Yoon, Gesine Saucke, Jürg Hulliger, and Anke Weidenkaff

Citation: Journal of Applied Physics **115**, 183704 (2014); doi: 10.1063/1.4874798
View online: http://dx.doi.org/10.1063/1.4874798
View Table of Contents: http://scitation.aip.org/content/aip/journal/jap/115/18?ver=pdfcov
Published by the AIP Publishing

Improved thermoelectric performance of $(Zr_{0.3}Hf_{0.7})NiSn$ half-Heusler compounds by Ta substitution

Krzysztof Gałązka,[1,2] Sascha Populoh,[1,a)] Wenjie Xie,[1] Songhak Yoon,[1] Gesine Saucke,[1] Jürg Hulliger,[2] and Anke Weidenkaff[1,3]
[1]*Laboratory for Solid State Chemistry and Catalysis, Empa, Überlandstrasse 129, CH-8600 Dübendorf, Switzerland*
[2]*Department of Chemistry and Biochemistry, University of Berne, Freiestrasse 3, CH-3012 Berne, Switzerland*
[3]*Materials Chemistry, Institute for Materials Science, University of Stuttgart, Heisenbergstr. 3, DE-70569 Stuttgart, Germany*

(Received 20 February 2014; accepted 22 April 2014; published online 12 May 2014)

The thermoelectric performance of Ta substituted (ZrHf)NiSn-based half-Heusler compounds is studied. Here, Ta is used on the Hf site for controlling the charge carrier concentration in contrast to the widely used Sb substitution on the Sn site. The influence of the Ta content on the thermoelectric and transport properties of $(Zr_{0.3}Hf_{0.7-x}Ta_x)NiSn$ ($x = 0$, 0.01, 0.05) is investigated by means of Seebeck coefficient, electrical resistivity, thermal conductivity, and Hall coefficient measurements. The results are analyzed in context of the single parabolic band model. Ta substitution increases the charge carrier concentration and suppresses the influence of impurity band, which is present in the pristine $(Zr_{0.3}Hf_{0.7})NiSn$. Moreover, Ta substitution decouples and simultaneously increases the density-of-states effective mass (m^*) and the charge carrier mobility (μ), leading to a larger weighted mobility $\mu \cdot (m^*)^{3/2}$. The lattice thermal conductivity is slightly suppressed due to increased point defect scattering. As a result, a Figure of Merit of 0.85 is achieved for $(Zr_{0.3}Hf_{0.65}Ta_{0.05})NiSn$ compound at 870 K, ca. 180% improvement over the unsubstituted sample. © *2014 AIP Publishing LLC*. [http://dx.doi.org/10.1063/1.4874798]

I. INTRODUCTION

Alternative energy sources are currently intensively investigated with the main focus on renewable, clean, and safe technologies. Most of the energy conversion processes involve production of heat which, in large part, is irreversibly lost. Recuperation of even a small portion of this wasted energy would have a tremendous impact on the overall energy production efficiency when applied on a global scale. Thermoelectricity offers the unique possibility of a direct solid state conversion of heat into electrical energy and could be a way to improve energy efficiency.

The efficiency of the thermoelectric conversion is ruled by the dimensionless Figure of Merit $ZT = \alpha^2 T/(\rho\kappa)$, where T is temperature, α the Seebeck coefficient, ρ electrical resistivity (or electrical conductivity $\sigma = \rho^{-1}$), and κ thermal conductivity.[1] A high ZT leads to a high conversion efficiency, therefore, the requirement for a good thermoelectric material is to exhibit large α, low ρ, and low $\kappa = \kappa_{latt} + \kappa_{carr}$, represented as sum of the lattice (κ_{latt}) and the carrier (κ_{carr}) contribution. However, α, ρ, and κ_{carr} are interrelated through the charge carrier concentration n and cannot be controlled independently.[2] This physical limitation led to the Phonon-Glass-Electron-Crystal (PGEC) concept, which aims to simultaneously minimize κ_{latt} and optimize n for a high Power Factor ($PF = \alpha^2/\rho$).[3]

Half-Heusler (HH) compounds exhibit a wide range of properties depending on their composition.[4] Recently, the XNiSn (X = Ti, Zr, Hf) HH compounds attracted interest of the thermoelectric community as promising thermoelectric materials in the temperature range of 700 K < T < 1200 K, suitable for waste heat recovery in industry. XNiSn HH compounds crystallize in $F\bar{4}3m$ space group symmetry. The elements with the highest difference in electronegativity, X and Sn, form a cubic rock salt lattice and Ni occupies the body center of each second XSn cube. Each atom site can be substituted for tuning the electron and phonon transport properties.[5] In the scope of the PGEC concept, the most successful strategies for improving the thermoelectric properties of XNiSn HH compounds have been: (1) isoelectric substitution on the X site with Ti and/or Zr and/or Hf to induce point defect scattering in order to suppress κ_{latt};[6–8] (2) Sb doping on the Sn site to adjust the carrier concentration for a high PF;[6,9,10] and (3) nanostructuring to limit the phonon mean free path and further suppress κ_{latt}.[11,12] Physical properties of the samples of the same nominal composition show considerable differences, as listed in Table I, raising questions about the influence of different synthesis methods on sample morphology and phase purity. The challenges for a reproducible synthesis are: the evaporation of the elements with low melting points (Sn and Sb) leading to non-stoichiometry; the appearance of secondary phases like Sn_5Ti_6 Ni_3Sn_4 or Sn;[13–15] and the miscibility limits of TiNiSn HH phase in ZrNiSn and in HfNiSn.[14,15] In this study, $(Zr_{0.3}Hf_{0.7})NiSn$ is chosen as a starting compound to exclude miscibility problems and limit secondary phases formation. The charge carrier concentration is tuned by Ta substitution instead of using low melting point Sb. Ta was found to raise the PF of $(Zr_{0.5}Hf_{0.5})NiSn$ about 7 times when substituted for 1% of Zr and Hf.[5] In TiCoSb, Ta substitution led to lower electrical

a)Author to whom correspondence should be addressed. Electronic mail: sascha.populoh@empa.ch

TABLE I. A summary of chosen literature data on thermoelectric properties of $Zr_yHf_{1-y}NiSn_{1-x}Sb_x$ HH compounds, where $y = [0.25, 0.5]$, $x = [0, 0.06]$ and a comparison to the examined $(Zr_{0.3}Hf_{0.7-x}Ta_x)NiSn$, where $x = 0$, 0.01, and 0.05.

				$(Zr_yHf_{1-y})NiSn_{1-x}Sb_x$				
References	y	x	PF_{MAX}(T/K)/mW/(K^2 m)	$(ZT)_{MAX}(T/K)$	$\kappa_{MIN}(T/K)$/W/(K m)	$n_H(300\,K)/10^{20}/cm^3$	$\mu_H(300\,K)/cm^2/(V{\cdot}s)$	m^*/m_e
	0.25	0.02	3.2(790)[a]	0.60(790)[a]	4.3(770)[a]	5.52	21.1	2.58
	0.25	0.04	3.2(470)	0.45(790)[a]	5.8(770)[a]	…	…	…
9	0.25	0.06	2.7(700)	0.30(790)[a]	7.3(770)[a]	…	…	…
	0.4	0.02	5.7(880)	1.00(1000)	4.1(770)	5.88	25.0	2.96
12	0.4	0.02	4.4(675)	0.70(880)	5.2(875)	10.0	18.3	3.5
21	0.4	0.02	3.7(780)	0.55(870)[a]	5.7(575)	10.3	18.7	3.3
10	0.5	0.01	5.2(773)	1.00(873)	3.9(673)	2.82	33.3	5.43[b]
	0.25	0.01	4.8(773)	0.95(873)	4.1(673)	2.5	37	4.84[b]
22	0.5	0.01	3.4(720)	0.60(800)	4.2(700)	…	…	…
23	0.35	0.02	…	0.5(875)	6.7(775)	5.2	28	2.9
	0.25	0	2.4(875)	…	…	0.55	16	1.5
24	0.25	0.01	3.0(750)	…	…	…	…	…
	0.25	0.03	4.5(925)	…	…	…	…	…
				$(Zr_yHf_{1-y-x}Ta_x)NiSn$				
	0.3	0	2.6(868)	0.30(870)	4.0(370)	0.29	26	0.52
	0.3	0.01	3.2(868)	0.70(870)	3.7(712)	0.94	38	1.69
	0.3	0.05	3.7(816)	0.85(870)	3.6(712)	2.37	35	2.29

[a]Value taken at the end of the measured temperature range, higher/lower values possible in an extended temperature range.
[b]Calculated from the reported values of n and α assuming alloy charge carrier scattering.

resistivity and a 5 times increase of the maximum *PF*.[16] Here, the thermoelectric performance of $(Zr_{0.3}Hf_{0.7-x}Ta_x)NiSn$ ($x = 0$, 0.01, and 0.05) is examined and compared to the results reported for Sb containing samples.

II. EXPERIMENTAL

Samples with the nominal compositions $Zr_{0.3}Hf_{0.7-x}Ta_x$ NiSn ($x = 0$, 0.01, 0.05) were prepared by arc melting in Ar (purity 99.9999%) from pure metals: Zr (Sigma Aldrich, 99.95% with nominal 3% Hf), Hf (Sigma Aldrich, 99.9% with nominal 3% Zr), Ni (Sigma Aldrich, 99.95+%), Sn (Sigma Aldrich, 99.99+%), and Ta (Fluka A.G., 99.7+%). Afterwards, the ingots were crushed and hand-ground into powders in an agate mortar and compacted by Spark Plasma Sintering (SPS, KCE®-FCT HP D 10). The SPS process was performed in 50 mbar overpressure of Ar (99.999%) after several flushing cycles, according to the procedure of previous studies found in the literature.[16] It comprised a heating ramp with 100 K/min and an 8 min isothermal step at $T = 1673$ K. During the whole procedure, 50 MPa of uniaxial pressure was applied. The temperature used for densification was set close to the melting point of ZrNiSn (1708 K, Ref. 17). As a result, disk-shaped pellets of about 2 mm thickness and 20 mm diameter were formed with densities higher than 99% of the theoretical value (measured both by the Archimedes method and by direct volumetric–gravimetric assessment).

The crystal structure and phase composition of the samples were assessed by powder X-Ray Diffraction (XRD, PANalytical X'Pert PRO). The diffractometer was equipped with a Johansson monochromator (Cu-Kα_1 radiation, 1.5406 Å) and an X'Celerator linear detector. Diffraction patterns were recorded between 20° and 100° (2θ) with an angular step interval of 0.0167°. The diffractograms were recorded before and after measuring the high temperature transport properties to confirm stability of the phase composition. The lattice parameters were determined by Le Bail fitting[18] using the program *FullProf*.[19] The Thompson-Cox-Hastings pseudo-Voigt function[20] was used as a profile function and CeO_2 (NIST SRM674b) was measured as a standard reference material to estimate the instrument-specific contribution to the peak broadening.

The morphology and phase composition of the samples were examined by Scanning Electron Microscopy (SEM, Philips ESEM-FEG XL30) with 20 kV acceleration voltage using a backscattered electron (BSE) detector. For SEM imaging, each sample was fine polished (Buehler, Vibromet 2) using a 50 nm MasterPrep polishing suspension (Buehler) and finally rinsed with de-ionized water and ethanol. The elemental mappings have been performed with energy dispersive X-ray spectroscopy (EDX) with 512×400 px^2 resolution (16 frames, 1 ms/px dwell time). The approximate stoichiometry was calculated from EDX point spectra.

The Hall resistivity ρ_H and the electrical resistivity ρ were measured with a Physical Properties Measurement System (PPMS, Quantum Design) using the Alternating Current Transport (ACT) option. The samples with approx. dimensions of $2 \times 2 \times 10$ mm^3 were connected in a four-probe configuration by using a wire bonder (FEK Devoltec 5425) with a 20 μm diameter Al wire to the ACT electrical interface.

Measurements were performed in a He-purged, evacuated chamber in the $5\,K < T < 400\,K$ temperature range with a 10 K step size. At each temperature, the magnetic field B was swept from -1 T to 1 T with 0.0015 T/s. The Hall coefficient R_H was then derived as the slope of the $\rho_H(B)$ dependence. The Hall charge carrier concentration n_H and the Hall mobility μ_H were calculated from $n_H = (R_H |e|)^{-1}$ and $\mu_H = R_H \rho^{-1}$, where $|e|$ is the absolute value of the elementary charge.

The high temperature electrical resistivity and the Seebeck coefficient were determined in the $325\,K < T < 1000\,K$ temperature range with a 50 K step size by using an RZ2001i unit (Ozawa Science). Measurements were performed in Ar (99.999%) on the samples used previously for the PPMS ACT measurements. The electrical resistivity was measured using a DC four-point method and the Seebeck coefficient was determined using a steady-state method.

The thermal conductivity was calculated from $\kappa = D \cdot d \cdot c_p$ using the experimental results for thermal diffusivity D, density d, and specific heat under constant pressure c_p. The thermal diffusivity was measured with a Laser Flash Apparatus (Micro Flash LFA 457, Netzsch) on square-shaped, graphite-coated samples with 10 mm side length. Measurements were done in Ar (99.999%) in the $323\,K < T < 1023\,K$ temperature range with a 50 K step. Specific heat c_p of the samples was measured by Differential Scanning Calorimetry (DSC, Netzsch Pegasus 404C) in the $400\,K < T < 1033\,K$ temperature range during heating with 10 K/min. The experiments were performed under 50 ml/min Ar (99.999%) flow by using Pt crucibles with an Al_2O_3 lining to prevent any alloying between the crucible and the sample. A Mo disk was used as a reference material and c_p was calculated by using the ratio method.

The thermal conductivity, electrical resistance, and Seebeck coefficient values were used to calculate the dimensionless Figure of Merit $ZT = \alpha^2 T/(\rho\kappa)$. A linear interpolation of the data was applied, when needed. The uncertainty of each measurement was calculated according to the exact differential method based on the systematic errors of the measured values and the double statistical standard deviation, where available.

III. RESULTS AND DISCUSSION

A. Structure and phase composition

The diffraction patterns of the synthesized samples are presented in Figure 1. All main reflexes are indexed according to the cubic $F\bar{4}3m$ space group symmetry. The main reflection (220) is enlarged in the inset of Figure 1. It clearly shows that the HH phase (labeled 1) has a shoulder (labeled 2) on the low-angle side. Therefore, two HH phases were used for the Le Bail fitting and the results are summarized in Figure 1. $(Zr,Hf)_5Sn_3$ and $(Zr,Hf)_2Ni_2Sn$ secondary phases were found and their amount is below 1%. Those secondary phases are visible in a SEM-BSE image of the $x = 0.01$ sample presented in Figure 2. The approximate composition of the main phase determined by EDX analysis is $(Zr_{0.3}Hf_{0.7})NiSn$ for all samples. The amount of secondary phases is roughly the same for each substitution level. A slight compositional difference between the grains of the main phase could be detected indicating a small excess of Ni over Sn in the darker grains compared to 1:1 stoichiometric ratio. The average grain size is approx. 80 μm. Ta distribution could not be resolved due to the small amount and EDX peak overlapping with Hf.

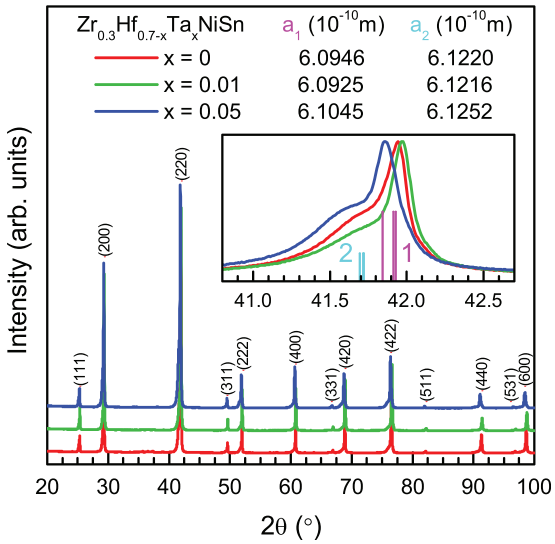

FIG. 1. XRD diffraction patterns of the synthesized samples. Peaks are indexed according to $F\bar{4}3m$ space group symmetry. The lattice parameters derived from the Le Bail fitting using a two HH phase model are listed. Inset presents the (220) reflection exposing its internal structure and overlapping peaks positions.

B. Electrical transport properties

The electrical resistivities of $(Zr_{0.3}Hf_{0.7-x}Ta_x)NiSn$ are presented in Figure 3(a). The unsubstituted sample exhibits

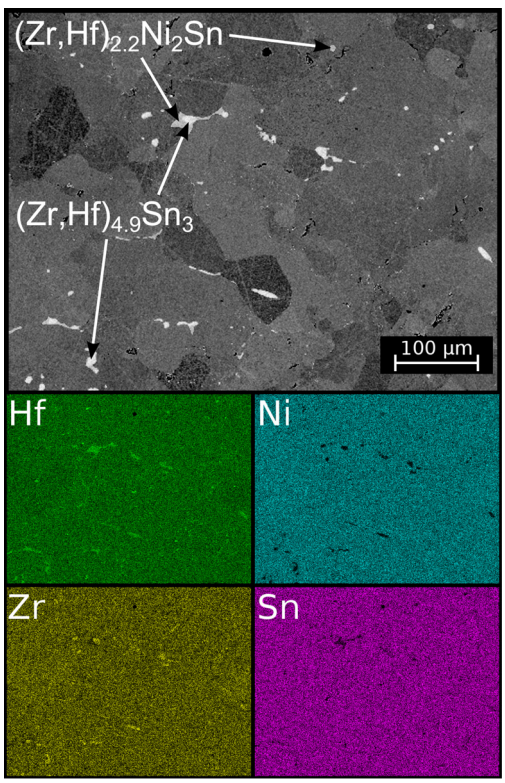

FIG. 2. SEM-BSE micrograph for the $x = 0.01$ sample together with EDX elemental mappings. The approximate stoichiometry was determined by EDX point spectra analysis.

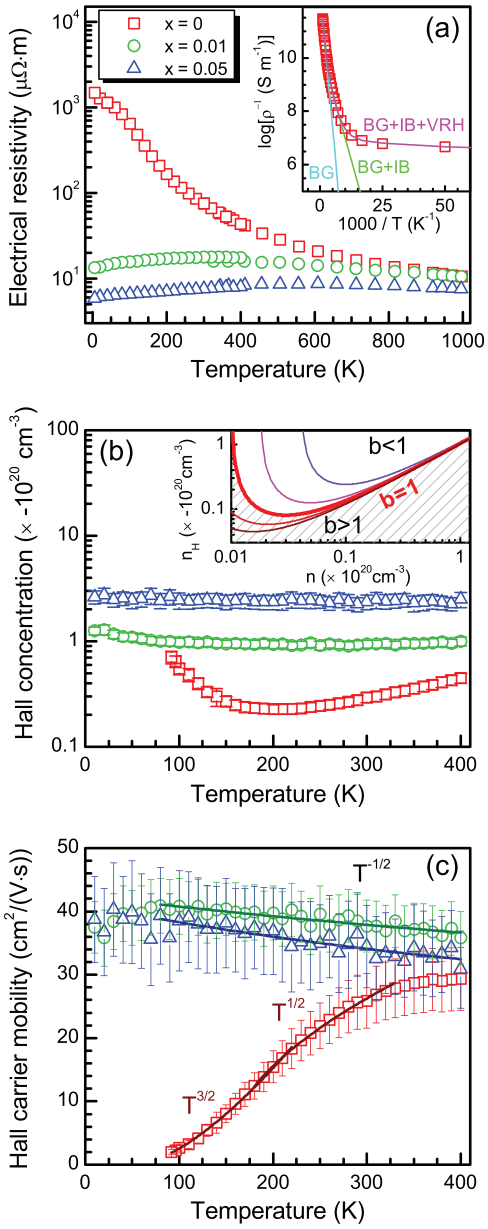

FIG. 3. (a) Electrical resistivity of the samples versus temperature. The measurement errors are smaller than the symbol size. Inset: Arrhenius plot for the unsubstituted sample and numerical fit by using combinations of three conduction mechanisms: EG—energy gap, IB—impurity band, VRH—variable range hoping. (b) Hall charge carrier concentration of the samples versus temperature. For the unsubstituted sample, it was possible to perform Hall measurement only down to 100 K. Inset: simulation of Hall concentration according to Eq. (5). By changing the value of b, the minimum of $n_H(n)$ occurs at lower ($b > 1$, shaded area) or higher ($b < 1$, clear area) values of n. (c) Hall mobility of the samples versus temperature.

semiconducting behavior in the whole temperature range, the inset of Figure 3(a) shows the Arrhenius plot. Three different electrical conduction models are adopted to explain the resistivity behavior of the $x = 0$ sample. At first, thermally activated conduction over an energy band gap (BG) is considered and fitted to the data. It is assumed that the resistivity follows the Arrhenius equation

$$\frac{1}{\rho} = \sigma_0 \exp\left(-\frac{\Delta E_0}{2k_B T}\right), \tag{1}$$

where ΔE_0 is a thermal band gap, σ_0 a pre-exponential factor, and k_B the Boltzmann constant. This model is valid for intrinsic semiconductors and for extrinsic ones in the high temperature limit. As it can be seen in the inset of Figure 3(a), it describes well the resistivity of the $x = 0$ sample at high temperature, but below $T = 500$ K the BG model starts to differ significantly from the experimental results. A more accurate description of the resistivity can be achieved assuming an impurity band (IB) situated within the band gap. The line labeled BG + IB in the inset of Figure 3(a) was fitted to the data following Eq. (2)

$$\frac{1}{\rho} = \sigma_0 \exp\left(-\frac{\Delta E_0}{2k_B T}\right) + \sigma_1 \exp\left(-\frac{\Delta E_1}{2k_B T}\right), \tag{2}$$

with an impurity activation energy ΔE_1 and pre-exponential factor σ_1. It extends the agreement between the model and the data down to about $T = 120$ K. The model can be further improved to better describe the $T < 120$ K temperature range by adding a term describing the variable range hoping (VRH) mechanism. The line labeled BG + IB + VRH is fitted according to Eq. (3) and shown in the inset of Figure 3(a)

$$\frac{1}{\rho} = \sigma_0 \exp\left(-\frac{\Delta E_0}{2k_B T}\right) + \sigma_1 \exp\left(-\frac{\Delta E_1}{2k_B T}\right) + \sigma_M \exp\left[-\left(\frac{T_M}{T}\right)^{1/4}\right]. \tag{3}$$

T_M and σ_M are the Mott temperature related to localization energy and a pre-exponential factor, respectively. The parameters derived for all three models are summarized in Table II.

ΔE_0 is different for each model. The discrepancy is especially large if the BG model is compared to the remaining two. The thermal band gap values resulting from the BG + IB and BG + IB + VRH models are close to the ones reported in the literature for similar compounds: 0.21 eV for ZrNiSn, 0.22 eV for $Zr_{0.25}Hf_{0.75}NiSn$, 0.24 eV for $Zr_{0.5}Hf_{0.5}NiSn$, and 0.33 eV for HfNiSn.[24,25] In this case, the simplest model leads to a significant underestimation of ΔE_0, despite a relatively small standard deviation. The existence of an impurity band in the unsubstituted sample with $\Delta E_1 \approx 0.02$ eV can be explained by interstitial defects or vacancies, since Zr-Sn or Hf-Sn antisite disorder was

TABLE II. Summary of the fitted parameters derived for different electrical resistivity models and their standard deviations.

	Model		
Parameters	BG	BG + IB	BG + IB + VRH
T range (K)	506–996	120–996	5–996
σ_0 (10^3 S·m^{-1})	260 ± 6	282 ± 4	274 ± 12
ΔE_0 (meV)	176 ± 3	242 ± 5	251 ± 16
σ_1 (10^3 S·m^{-1})	…	37 ± 3	46 ± 9
ΔE_1 (meV)	…	16 ± 2	20.0 ± 0.9
σ_M (10^3 S·m^{-1})	…	…	2 ± 1
T_M (K)	…	…	17 ± 58

demonstrated to lead to band gap narrowing.[4,26] The nature of the impurity band is discussed below with respect to the charge carrier concentration.

VRH has been already observed in ZrNiSn (Refs. 27 and 28) and other HH systems (e.g., YPdSb,[29] ZrCoSb, and NbFeSb[30]). It is related to the charge carrier localization at low temperatures.[31] If an impurity band is present, VRH can originate from a smaller overlap of the electron wave functions of impurity atoms at low temperatures.[28,32] A $T_M = 17$ was found, however, with a large standard deviation. Other reported T_M values are 87 K for NbFeSb,[30] 0.6 K for YPdSb,[29] 0.26 K for TbNiSb, and 0.24 K for HoNiSb.[33] A more precise analysis of the VRH mechanism would require the acquisition of additional data points in the $1\,\mathrm{K} < T < 100\,\mathrm{K}$ temperature range, which is beyond the scope of this paper.

For the Ta-substituted samples, both of them show metallic-like transport behavior in the low temperature range (Figure 3(a)). The electrical resistivity for the $x = 0.01$ sample reaches a flat maximum at about $T = 330\,\mathrm{K}$, and then the slope becomes negative. A similar behavior is observed for the $x = 0.05$ sample, but with the maximum shifted to $T = 580\,\mathrm{K}$. Similar behavior was reported for Ta-substituted TiCoSb.[16] The substitution is most effective at low temperatures, where the resistivity is lowered by more than one order of magnitude.

Hall charge carrier concentration is presented in Figure 3(b). For the unsubstituted sample, n_H shows a non-monotonous behavior: initially, it decreases with the temperature reaching minimum at $T = 210\,\mathrm{K}$ and then starts to increase again. The Hall coefficient in a mixed semiconductor is expressed by

$$\frac{1}{|e|n_H} = R_H = \frac{r_H\left(p\mu_h^2 - n\mu_e^2\right)}{|e|(p\mu_h + n\mu_e)^2}, \tag{4}$$

where p stands for the hole concentration in the valence band, n for the electron concentration in the conduction band, and μ_h and μ_e for electron and hole mobilities, respectively.[34] The Hall factor r_H is a constant in the order of unity, which depends on the involved electron scattering processes.[35] In large band gap n-type semiconductors where the Fermi level lies far from the edge of valence band $n \gg p$ and R_H is negative, which gives negative $n_H \approx -n$. However, in small band gap semiconductors already at relatively low temperatures p can be sufficiently large compared to n to play a role in Eq. (4). When the conditions are close to degeneracy (n higher than 10^{18}), the minority charge carrier concentration is weakly temperature dependent[34] and can be regarded constant. From Eq. (4) follows that (for simplicity $r_H = 1$)

$$n_H \propto \frac{(p + nb)^2}{p - nb^2}, \tag{5}$$

where $\mathrm{b} = \mu_e/\mu_h$ is the mobility ratio. The inset of Figure 3(b) presents a calculation assuming $p = 10^{18}\,\mathrm{cm}^{-3}$ and n changing in the 10^{18}–$10^{20}\,\mathrm{cm}^{-3}$ range for different values of b. The parameters are set in a way that the calculated n_H dependence reflects the activation of the impurity level. Using $\log(n)$ instead of T as an ordinate is justified since in an activated behavior n rises monotonically with T. It is remarkable that in this simplified model n_H has a non-monotonous behavior, as in experimental results. The thermal energy corresponding to the minimum of n_H of the unsubstituted sample (Figure 3(b)) $k_B \cdot 210\,\mathrm{K} = 18\,\mathrm{meV}$ is comparable to the impurity band activation energy $\Delta E_1 = 20\,\mathrm{meV}$ (Table II).

As aforementioned, the impurity band can originate from structural defects like interstitials or vacancies. According to the theoretical calculations, in case of TiNiSn Ni is the most probable element to form defects.[36] Usually, the defect formation is reflected by a change in the lattice parameter. Comparing the lattice parameters derived from Le Bail fitting (Figure 1) to the reported lattice parameters $a_{ZrNiSn} = 6.113$ Å and $a_{HfNiSn} = 6.083$ Å for pure ZrNiSn and HfNiSn, respectively,[37] it is found that $a_{HfNiSn} < a_1 < a_{ZrNiSn} < a_2$. According to Vegards law, the lattice parameter of a solid solution is limited by the end compositions. Thus, it is obvious that the expanded lattice parameter (a_2) cannot originate from the formation of a solid solution between ZrNiSn and HfNiSn but rather from defects. In case of TiNiSn interstitial, Ni is predicted to lead to n-type behavior.[36] Similar calculations for (Zr,Hf)NiSn would be greatly demanded to confirm the experimental data. The impurity charge carrier concentration is of great importance for the thermoelectric properties and can be a reason for the discrepancies between the reported transport properties of HH compounds (c.f. Table I).

For the substituted samples, the Hall carrier concentration is increased and is nearly temperature independent, indicating degeneracy. Slight influence of the impurity band is still visible for the $x = 0.01$ sample, but the $x = 0.05$ sample shows constant n_H in the whole measured temperature range. The room temperature Hall carrier concentration values are $-0.9 \times 10^{20}\,\mathrm{cm}^{-3}$ ($3.2 \times n_H$ for $x = 0$) and $-2.4 \times 10^{20}\,\mathrm{cm}^{-3}$ ($8.17 \times n_H$ for $x = 0$) for the $x = 0.01$ and $x = 0.05$ samples, respectively. These are close to the predicted optimal value for a similar $Zr_{0.5}Hf_{0.5}NiSn$ system,[38] which at room temperature is $-1.62 \times 10^{20}\,\mathrm{cm}^{-3}$. Similar n_H to the one of $x = 0.05$ sample was achieved in nanostructured $Zr_{0.25}Hf_{0.75}NiSn$ and $Zr_{0.5}Hf_{0.5}NiSn$ by 1% Sb substitution on the Sn site.[10] The estimated doping efficiency based on $n_H(300\,\mathrm{K})$ values is 50%—each two Ta atoms contribute one electron to the conduction band, whereas the other one reduces the free hole density, in agreement with basic semiconductor theory.[39]

The temperature dependence of the Hall mobility is presented in Figure 3(c). The scattering parameter r (single relaxation time approximation) can be estimated from the exponent of $\mu_H \sim T^r$. For the unsubstituted sample below 200 K, ionized impurity scattering with $r = 3/2$ is dominant.[40] This corresponds to the temperature range in which the impurity band gives the main contribution to the conductivity. The inflection point at $T \approx 200\,\mathrm{K}$ corresponds to the minimum in n_H (see Figure 3(b)) and indicates the onset of the depletion of the impurity levels. In the $200\,\mathrm{K} < T < 325\,\mathrm{K}$ temperature range, the mechanism changes and $r = 1/2$, i.e., polar scattering on optical phonons becomes dominant.[40]

This scattering process was claimed to be relevant for HH phases with low charge carrier concentrations (below $10^{20}\,cm^{-3}$).[23] Above $T = 325\,K$ r changes again, however, the temperature range is too small to identify the $\mu_H(T)$ dependency. For both of the substituted samples in the $90\,K < T < 400\,K$ temperature range $r = -1/2$ was found which corresponds to alloy scattering.[40] All samples exhibit relatively high Hall mobility values at room temperature (c.f. Table I). The closest reported value is 37 $cm^2/(V\,s)$ for the nanostructured $Hf_{0.75}Zr_{0.25}NiSn_{0.99}Sb_{0.01}$. Increasing the Sb content from 1% to 2% and more lowers the carrier mobility, while for Ta substitution high μ_H values are preserved.

C. Analysis of the high temperature thermoelectric properties in scope of the single parabolic band (SPB) model

The negative Seebeck coefficient presented in Figure 4(a) confirms n-type conduction for all samples. α is gradually decreasing (in terms of absolute values) with increasing substitution, which is consistent with the basic derivation of $\alpha \sim \ln(1/n)$ in the non-degenerated SPB model.[34] It can be noted that with substitution the maximum of the absolute value of the Seebeck coefficient is shifted to higher temperatures, from $T = 575\,K$ for $x = 0$ to around $T = 678\,K$ for $x = 0.01$ and to $T = 764\,K$ for the $x = 0.05$. In general, the Seebeck coefficient reaches a maximum (or a minimum) due to the increasing contribution of the minority carriers at high temperatures.[41] A shift of the peak position of α towards higher temperatures indicates that the contribution of minority carriers is smaller at higher Ta substitution levels. It corresponds to a higher position of the Fermi level, in agreement with previous observations (see Figure 3).

The band gap estimated from $2e{\cdot}T_{MAX}{\cdot}|\alpha_{MAX}|$ (Ref. 41) is 236 meV for the unsubstituted sample, which is in good agreement with the thermal band gap (see Table II). The values for the substituted ones are higher: 273 meV for $x = 0.01$ and 272 meV for $x = 0.05$ suggesting a widening of the band gap for the Ta-substituted samples. However, the expression used was derived for a non-degenerated semiconductor assuming equal effective masses for holes and electrons, so the last two results are only rough approximations.

According to Boltzmann transport theory in the SPB model (single relaxation time approximation), charge carrier concentration, Seebeck coefficient, and Lorenz number L are given by

$$n = 4\pi \cdot \left(\frac{2m^* k_B T}{h^2}\right)^{\frac{3}{2}} \cdot F_{1/2}(\eta_F), \tag{6}$$

$$\alpha = \frac{k_B}{e}\left(\eta_F - \frac{r + 5/2}{r + 3/2} \cdot \frac{F_{r+3/2}(\eta_F)}{F_{r+1/2}(\eta_F)}\right), \tag{7}$$

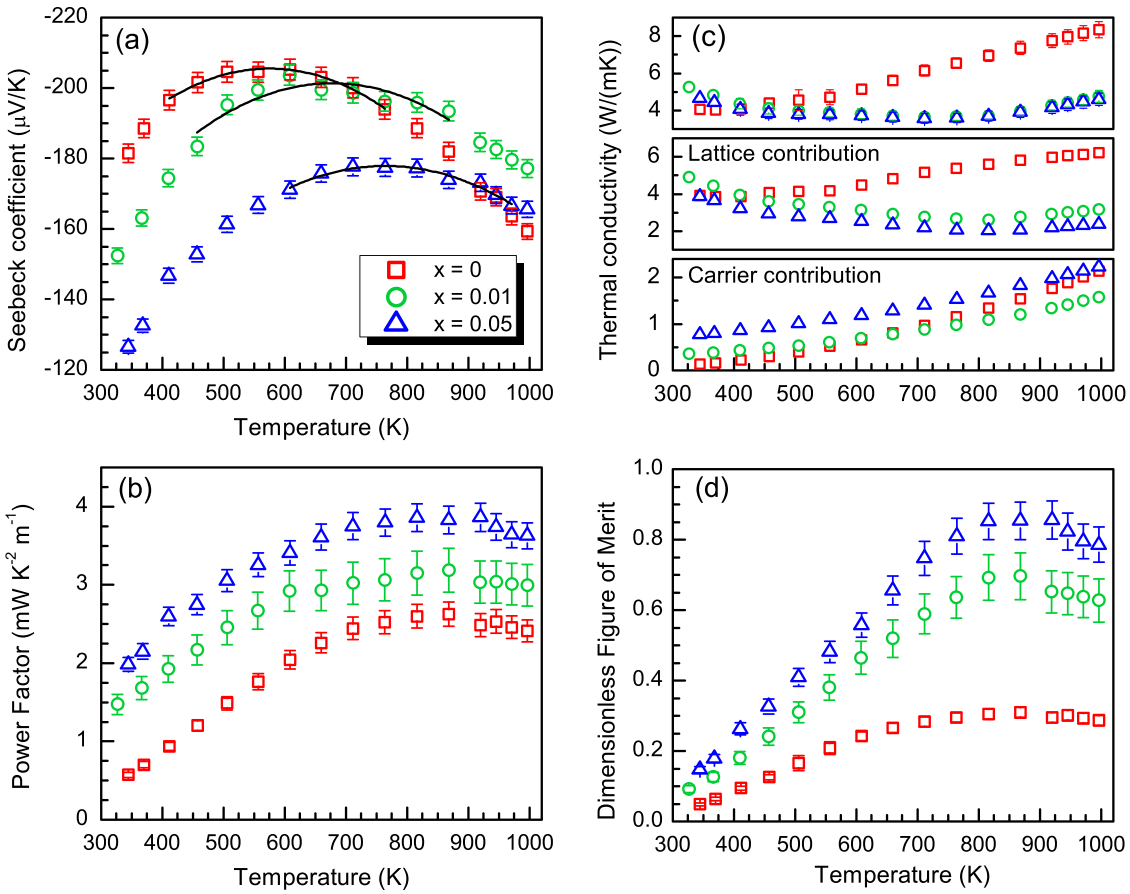

FIG. 4. (a) The Seebeck coefficient of the samples versus temperature. Parabolic fits allowed determining the peak positions. (b) The Power Factor versus temperature. (c) The thermal conductivity versus temperature. (d) The dimensionless Figure of Merit versus temperature.

$$L = \left(\frac{k_B}{e}\right)^2 \cdot \frac{(r+7/2)(r+3/2)F_{r+5/2}(\eta_F)F_{r+1/2}(\eta_F) - (r+5/2)^2\left[F_{r+3/2}(\eta_F)\right]^2}{(r+3/2)^2\left[F_{r+1/2}(\eta_F)\right]^2}, \quad (8)$$

where m^* is the density-of-states effective mass, h the Planck's constant, $\eta_F = E/(k_BT)$ the reduced Fermi energy and

$$F_s(\eta_F) = \int_0^\infty \frac{\eta^s}{1+e^{\eta-\eta_F}} d\eta \quad (9)$$

denotes the complete Fermi-Dirac integral of order s. Using the scattering parameter $r = 1/2$ for the unsubstituted sample and $r = -1/2$ for the substituted ones (c.f. Figure 3(c)), the effective charge carrier mass was calculated at $T = 300$ K and presented in unit of free electron mass m_e in Table I. For all samples, m^* is in the order of m_e, in rough agreement with previous research (see Table I). According to $m^* = \hbar^2/(d^2E/dk^2)$, where k stands for the wave vector, E for the energy of the charge carriers, and $\hbar$ is the reduced Planck's constant, a larger m^* results in a lower slope of the energy dispersion curve and "flatter" bands. DOS calculations show that the conduction band of XNiSn compounds is dominated by the d-electrons of the X element.[36,42] Here, similarly to V doping in $(Zr_{0.25}Hf_{0.75})NiSn$,[24] Ta substitution on the X site does not only increase the charge carrier concentration but also changes the DOS.

Expanding $ZT = \alpha^2T/(\rho\kappa)$ by using expressions for α, ρ, and κ_{carr} derived from the SPB model leads to a dimensionless quality factor $\beta = 5.745 \times 10^{-6} \times \mu \cdot (m^*/m_e)^{3/2} \cdot T^{5/2}/\kappa_{latt}$.[40] Accordingly, the thermoelectric efficiency is improved by maximizing the weighted mobility, $\mu \cdot (m^*/m_e)^{3/2}$. Deformation potential theory predicts that generally μ is inversely proportional to m^*.[23,43] In the case of Ta substitution, it was possible to decouple m^* and μ—for the substituted samples both parameters are enhanced. The beneficial effects of Ta substitution on n, μ, and m^* are clearly reflected as an enhancement of the Power Factor in the whole measured temperature range (Figure 4(b)). For all samples, the maxima of broad peaks are between 750 K and 950 K and the values are 2.6×10^{-3} W/(K m) for the unsubstituted sample, 3.2×10^{-3} W/(K m) for $x = 0.01$ (23% increase), and 3.9×10^{-3} W/(K m) for the $x = 0.05$ sample (50% increase). The values are comparable to the ones achieved by Sb substitution in similar compounds (c.f. Table I).

The thermal conductivity of the samples is presented in Figure 4(c). For all samples, the behavior is similar: κ diminishes with increasing temperature and after reaching a minimum the total thermal conductivity increases due to the growing contribution of the κ_{carr}. For the unsubstituted sample, the minimum is reached already at 370 K. Both of the substituted samples have the minimum κ shifted to around 710 K. To get a better insight, κ_{carr} was calculated from the Wiedemann-Franz relationship $\kappa_{carr} = LT/\rho$ using the Lorenz number calculated according to Eq. (8) (for the $x = 0$ sample $r = 1/2$ was used, for the other two $r = -1/2$, according to the analysis of the temperature dependence of μ_H). The lattice part of the thermal conductivity κ_{latt} is derived by subtracting κ_{carr} from κ and the results are presented in Figure 4(c). For all samples, κ_{latt} exhibits the same trend with an up-turn at about 410 K for the unsubstituted sample and around 815 K for the substituted ones. In agreement with the Seebeck coefficient results (Figure 4(a)), this shows that the influence of the minority charge carriers at high temperatures cannot be neglected and underlines the limits of the approximations used.

Although at temperatures above the minority charge carrier excitation, the calculated Lorenz number is not valid anymore, the results for the substituted samples below the onset of the bipolar effect can be discussed. The lowered values of κ_{latt} for the $x = 0.05$ sample suggest higher phonon scattering by point defects due to mass and strain fluctuations. However, for $T > 100$ K Umklapp-scattering by phonon-phonon interaction becomes dominant, weakening the effect of Ta substitution. The higher contribution of κ_{carr} for the $x = 0.05$ sample is a direct consequence of higher charge carrier concentration (for both substituted samples L is in the range of 1.6–1.8 WΩ K^{-2} at all temperatures) and the reduced κ_{latt} values can be attributed to increased phonon-electron interaction ratio.[23]

In general, κ values are in a range typical for HH compounds with isoelectronic substitution on the X site.[6,8] Ta-substituted compounds show κ values comparable to nanostructured Sb-substituted (Zr,Hf)NiSn.[10] Even lower thermal conductivity should be expected when the grain size and shape are refined.

The resulting Figure of Merit is presented in Figure 4(d). The maximum ZT value of 0.85 is achieved for $Zr_{0.3}Hf_{0.65}Ta_{0.05}NiSn$ at 870 K. The improvement with regards to the unsubstituted sample ($ZT_{MAX} = 0.3$) is 133% for the $x = 0.01$ sample and 183% for the $x = 0.05$ one. It can be concluded that ZT is enhanced for the substituted samples owing to decoupling and simultaneous increase of the carrier mobility and the effective mass. This fact is illustrated in Figure 5 for all samples at $T = 400$ K. Considering the expression for the conductivity mobility $\mu = e\tau/m^*$

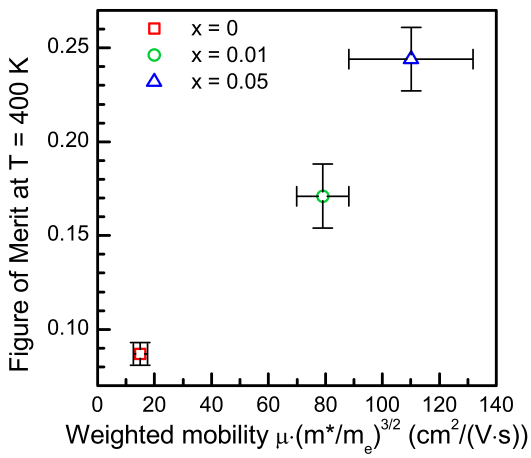

FIG. 5. The dimensionless Figure of Merit versus weighted mobility at 400 K.

($\mu = \mu_H/r_H$ where $r_H \approx 1$) from the classical electron gas theory,[44] the increased weighted mobility corresponds to an increased charge carrier relaxation time τ. The negative influence of minority charge carriers is suppressed due to an increased n-type charge carrier concentration. At the same time, increased phonon scattering due to Ta-induced point defects slightly lowers the lattice thermal conductivity. It is a particular case that a single dopant has so many beneficial effects on the thermoelectric properties of a material. Further improvement of *ZT* can be enabled by eliminating the impurity band, limiting κ_{latt}, i.e., through nanostructuring, grain shape refinement,[10] or alternative charge transport control methods, e.g., through nanoinclusions.[45,46]

IV. CONCLUSIONS

HH compounds with the formula $(Zr_{0.3}Hf_{0.7-x}Ta_x)NiSn$ ($x = 0$, 0.01, 0.05) were synthesized and their thermoelectric properties investigated in terms of the SPB model in single relaxation time approximation. The electrical resistivity and Hall charge carrier concentration results analysis indicate the existence of an impurity band within the band gap, possibly resulting from Ni interstitial defects. By Ta substitution, it was possible to suppress the negative effect of the minority carriers as well as to decouple normally correlated parameters, namely carrier mobility and effective mass. The charge carrier concentration was successfully adjusted with an estimated doping efficiency of 50%. Moreover, thermal conductivity of the Ta-containing compounds was lowered due to increased phonon scattering. The results show that Ta is a promising, easy-controllable, non-toxic dopant and a good alternative to Sb. New perspectives are expected to open by application of grain shape and size refinement or incorporation of secondary nano-sized phase.

ACKNOWLEDGMENTS

The authors gratefully acknowledge Swisselectric and the Deutsche Forschungsgesellschaft within the DFG Priority Program SPP 1386 for financial support. W.X. would like to thank the Marie Curie COFUND fellowship supported by EU FP7 and EMPA.

[1]D. J. M. Rowe, in *Thermoelectrics Handbook*, edited by D. J. M. Rowe (CRC Press, Boca Raton, 2006).
[2]G. J. Snyder and E. S. Toberer, Nature Mater. **7**, 105 (2008).
[3]G. A. Slack, in *CRC Handbook of Thermoelectrics*, edited by D. J. M. Rowe (CRC Press, Boca Raton, 1995), p. 407.
[4]T. Graf, C. Felser, and S. Parkin, Prog. Solid State Chem. **39**, 1 (2011).
[5]H. Hohl, A. P. Ramirez, C. Goldmann, G. Ernst, B. Wölfing, and E. Bucher, J. Phys.: Condens. Matter **11**, 1697 (1999).
[6]C. Uher, J. Yang, S. Hu, D. T. Morelli, and G. P. Meisner, Phys. Rev. B **59**, 8615 (1999).
[7]N. Shutoh and S. Sakurada, J. Alloys Compd **389**, 204 (2005).
[8]S. Populoh, M. H. Aguirre, O. C. Brunko, K. Galazka, Y. Lu, and A. Weidenkaff, Scr. Mater. **66**, 1073 (2012).
[9]C. Yu, T. J. Zhu, R. Z. Shi, Y. Zhang, X. B. Zhao, and J. He, Acta Mater. **57**, 2757 (2009).
[10]S. Chen, K. C. Lukas, W. Liu, C. P. Opeil, G. Chen, and Z. Ren, Adv. Energy Mater. **3**, 1210 (2013).
[11]G. Joshi, X. Yan, H. Z. Wang, W. S. Liu, G. Chen, and Z. F. Ren, Adv. Energy Mater. **1**, 643 (2011).
[12]C. Yu, T. J. Zhu, K. Xiao, J. J. Shen, S. H. Yang, and X. B. Zhao, J. Electron. Mater. **39**, 2008 (2010).
[13]A. Berche, J.-C. Tedenac, and P. Jund, private communication (Waldeck, 2013).
[14]T. Kenjo, Y. Kimura, and Y. Mishima, in *Material Research Society Fall Meeting 2009*, edited by H. Radousky, J. Holbery, L. Lewis, and F. Schmidt (Cambridge University Press, Boston, MA, 2010), Vol. 1218.
[15]K. Gałązka, S. Populoh, L. Sagarna, L. Karvonen, W. Xie, A. Beni, P. Schmutz, J. Hulliger, and A. Weidenkaff, Phys. Status Solidi A (published online).
[16]M. Zhou, L. D. Chen, C. D. Feng, D. L. Wang, and J. F. Li, J. Appl. Phys. **101**, 113714 (2007).
[17]D. Jung, K. Kurosaki, C. Kim, H. Muta, and S. Yamanaka, J. Alloys Compd. **489**, 328 (2010).
[18]A. Le Bail, H. Duroy, and J. L. Fourquet, Mater. Res. Bull. **23**, 447 (1988).
[19]J. Rodríguez-Carvajal, Physica B **192**, 55 (1993).
[20]P. Thompson, D. E. Cox, and J. B. Hastings, J. Appl. Crystallogr. **20**, 79 (1987).
[21]T. J. Zhu, K. Xiao, C. Yu, J. J. Shen, S. H. Yang, A. J. Zhou, X. B. Zhao, and J. He, J. Appl. Phys. **108**, 044903 (2010).
[22]Q. Shen, L. Chen, T. Goto, T. Hirai, J. Yang, G. P. Meisner, and C. Uher, Appl. Phys. Lett. **79**, 4165 (2001).
[23]H. H. Xie, H. Wang, Y. Z. Pei, C. G. Fu, X. H. Liu, G. J. Snyder, X. B. Zhao, and T. J. Zhu, Adv. Funct. Mater. **23**, 5123 (2013).
[24]J. W. Simonson, D. Wu, W. J. Xie, T. M. Tritt, and S. J. Poon, Phys. Rev. B **83**, 235211 (2011).
[25]B. A. Cook, G. P. Meisner, J. Yang, and C. Uher, in *Proceedings of Eighteenth International Conference on Thermoelectrics, ICT'99* (1999), p. 64.
[26]S. Ogut and K. M. Rabe, Phys. Rev. B **51**, 10443 (1995).
[27]F. G. Aliev, N. B. Brandt, V. V. Moshchalkov, V. V. Kozyrkov, R. V. Skolozdra, and A. I. Belogorokhov, Z. Phys. B: Condens. Matter **75**, 167 (1989).
[28]E. Arushanov, W. Kaefer, K. Fess, C. Kloc, K. Friemelt, and E. Bucher, Phys. Status Solidi A **177**, 511 (2000).
[29]K. Gofryk, D. Kaczorowski, T. Plackowski, J. Mucha, A. Leithe-Jasper, W. Schnelle, and Y. Grin, Phys. Rev. B **75**, 224426 (2007).
[30]G. Melnyk, E. Bauer, P. Rogl, R. Skolozdra, and E. Seidl, J. Alloys Compd. **296**, 235 (2000).
[31]N. F. Mott, Philos. Mag. **19**, 835 (1969).
[32]N. F. Mott and W. D. Twose, Adv. Phys. **10**, 107 (1961).
[33]J. Pierre and I. Karla, J. Magn. Magn. Mater. **217**, 74 (2000).
[34]A. F. Ioffe, *Fizika Poluprovodnikov* (Publishing House of USSR, Moscow, 1957).
[35]K. Seeger, *Semiconductor Physics*, 9th ed., 2004 ed. (Springer-Verlag, Berlin, 2004), Vol. 1.
[36]C. Colinet, P. Jund, and J.-C. Tedenac, Intermetallics **46**, 103 (2014).
[37]W. Jeitschko, Metall. Trans. **1**, 3159 (1970).
[38]D. F. Zou, S. H. Xie, Y. Y. Liu, J. G. Lin, and J. Y. Li, J. Appl. Phys. **113**, 193705 (2013).
[39]J. S. Blakemore, *Semiconductor Statistics* (Dover Publications, Inc., New York, 1987).
[40]G. S. Nolas, J. Sharp, and H. J. Goldsmid, *Thermoelectrics: Basic Principles and New Materials Developments* (Springer, Berlin, 2001).
[41]H. J. Goldsmid and J. W. Sharp, J. Electron. Mater. **28**, 869 (1999).
[42]M. Hichour, D. Rached, R. Khenata, M. Rabah, M. Merabet, A. H. Reshak, S. Bin Omran, and R. Ahmed, J. Phys. Chem. Solids **73**, 975 (2012).
[43]J. Bardeen and W. Shockley, Phys. Rev. **80**, 72 (1950).
[44]W. C. Dunlap, *An Introduction to Semiconductors* (John Wiley & Sons, Inc., New York, 1957).
[45]W. J. Xie, Y. G. Yan, S. Zhu, M. Zhou, S. Populoh, K. Galazka, S. J. Poon, A. Weidenkaff, J. He, X. F. Tang, and T. M. Tritt, Acta Mater. **61**, 2087 (2013).
[46]W. J. Xie, J. He, S. Zhu, X. L. Su, S. Y. Wang, T. Holgate, J. W. Graff, V. Ponnambalam, S. J. Poon, X. F. Tang, Q. J. Zhang, and T. M. Tritt, Acta Mater. **58**, 4705 (2010).